https://doi.org/10.5194/egusphere-2026-5052
Preprint. Discussion started: 8 September 2026


# Combustion controls and plume structure of wildfire aerosol optical properties observed by TROPOMI

Barbara Dix[1], Lindsey D. Anderson[1,2*], J. Pepijn Veefkind[3,4], and Joost de Gouw[1,2]

[1] Cooperative Institute for Research in Environmental Sciences, University of Colorado Boulder, Boulder, CO, 80309, USA
[2] Department of Chemistry, University of Colorado Boulder, Boulder, CO, 80309, USA
[3] Royal Netherlands Meteorological Institute (KNMI), De Bilt, 3731 GA, The Netherlands
[4] Department of Civil Engineering and Geosciences, Technical University of Delft, Delft, 2600 AA, Netherlands
[*] now at Department of Chemistry and Biochemistry, University of California Los Angeles, Los Angeles, CA, 90095, USA

*Correspondence to*: Barbara Dix (barbara.dix@colorado.edu)

**Abstract.** Wildfire smoke influences air quality and climate through the scattering and absorption of solar radiation by aerosol particles, yet the factors controlling aerosol optical properties and their spatial variability within smoke plumes remain uncertain. Here, we use satellite observations of aerosol optical properties and trace gases from the TROPOspheric Monitoring Instrument (TROPOMI) to investigate the influence of combustion conditions on aerosol optical properties and their spatial variability within wildfire smoke plumes during the Australian 2018–2019 and 2019–2020 bushfire seasons. Substantial differences in aerosol optical depth (AOD) and single-scattering albedo (SSA) are observed among major land cover types. Wildfires characterized by stronger flaming combustion, inferred from nitrogen dioxide ($NO_2$) and carbon monoxide (CO) column density ratios ($\Delta NO_2/\Delta CO$), are associated with more absorbing plume-averaged aerosol populations, whereas smoldering-dominated fires are associated with more scattering smoke and larger AOD. These relationships indicate that combustion conditions exert a first-order control on aerosol absorptivity, while aerosol loading is more strongly influenced by total emissions. Within individual plumes, aerosol loading and trace gas abundance remain concentrated in $NO_2$-defined plume cores, whereas SSA exhibits much weaker spatial gradients. Independent box-size analyses further show a systematic tendency toward higher SSA away from plume cores and source regions while $\Delta NO_2/\Delta CO$ decreases, indicating that these spatial changes occur concurrently with atmospheric processing. Although chemical processing, dilution, and mixing cannot be separated, these observations provide constraints for evaluating model representations of wildfire emissions, plume evolution, and smoke radiative effects.

## 1 Introduction

Biomass burning is a major source of aerosols to the global atmosphere (Akagi et al., 2011; Andreae, 2019). Wildfire aerosols are harmful to human health and affect atmospheric chemistry and climate directly by scattering and absorbing solar radiation, and indirectly by modifying cloud properties (Bond et al., 2013; Reid et al., 2016; IPCC, 2021). Their importance is expected to increase as climate change enhances the frequency, intensity, and duration of wildfires in many regions of the world, leading

https://doi.org/10.5194/egusphere-2026-5052
Preprint. Discussion started: 8 September 2026


to larger aerosol emissions and more frequent long-range smoke transport events (Jolly et al., 2015; IPCC, 2021; Jones et al., 2022).

Wildfire smoke consists of complex mixtures of primary particulate emissions, including black carbon (BC), often referred to as soot, and organic carbon (OC) aerosol. During transport, smoke aerosols undergo physical and chemical evolution driven by dilution, condensation, coagulation, water uptake, and the formation of secondary organic aerosol (SOA) from oxidation of volatile organic compounds (Andreae, 2019; Reid et al., 2005a). These processes modify aerosol size distributions, composition, and optical properties over timescales of hours to days. Consequently, the radiative effects of wildfire smoke remain a major source of uncertainty in assessments of aerosol-radiation interactions and climate forcing (IPCC, 2021).

Numerous aircraft and ground-based studies have documented the rapid optical evolution of fresh smoke plumes (Palm et al., 2020; Reid et al., 2005b). However, these observations typically sample a limited number of plumes over relatively short time periods, making it difficult to establish relationships across diverse fuel types, combustion conditions, and stages of plume evolution. Satellite observations complement these measurements by providing large ensembles of wildfire plumes sampled under a wide range of environmental conditions, enabling statistical investigation of the factors controlling aerosol optical properties. Furthermore, smoke plumes generally remain internally heterogeneous during the first several hours after emission. Consequently, the spatial distributions of aerosol and trace gas properties within individual plumes can provide additional information on the coupled effects of atmospheric processing and mixing.

Recent advances in satellite remote sensing have demonstrated that wildfire smoke observations contain valuable information on wildfire emissions, land cover type, combustion conditions and plume chemistry. Measurements of carbon monoxide (CO), nitrogen dioxide ($NO_2$), and nitrous acid (HONO) from the TROPOspheric Monitoring Instrument (TROPOMI) have been used to constrain $NO_2$ and CO emissions (Griffin et al., 2021, 2024), while trace gas column ratios of $\Delta NO_2/\Delta CO$ have been applied to distinguish between more flaming and more smoldering combustion and infer information on land cover type (Anderson et al., 2023; van der Velde et al., 2021). The ratio of HONO to $NO_2$ has been used to investigate relationships between fire radiative output and atmospheric chemical processing (Fredrickson et al., 2023). These studies suggest that trace gas observations contain information not only on wildfire emissions, but also on the processes that govern the composition and atmospheric processing of smoke plumes.

Fresh smoke emitted during flaming combustion typically contains larger fractions of BC, whereas smoldering combustion produces larger amounts of OC aerosols that contribute primarily to scattering (Andreae, 2019; Bond et al., 2013; Reid et al., 2005b). Consequently, combustion conditions are expected to influence both aerosol loading and aerosol absorptivity, as well as their subsequent changes during atmospheric transport. An important remaining question is to what extent the combustion signatures and spatial patterns identified in trace gas observations are also reflected in aerosol optical properties, and whether aerosol observations provide complementary constraints on wildfire combustion and atmospheric processing.

The Australian 2018–2019 and 2019–2020 bushfire seasons provide an ideal opportunity to address this question because they encompass a large ensemble of wildfire plumes spanning diverse land cover types and combustion conditions. In addition, Australia's relatively sparse population density facilitates the separation of wildfire emissions from anthropogenic pollution.

https://doi.org/10.5194/egusphere-2026-5052
Preprint. Discussion started: 8 September 2026


The 2019–2020 season, commonly referred to as the "Black Summer," was characterized by extreme temperatures and prolonged drought that contributed to a fire season of unprecedented scale, with substantial impacts on tropospheric and stratospheric composition, regional climate, and air quality (Boer et al., 2020; Khaykin et al., 2020).

To investigate these fires, we combined coincident TROPOMI observations of $NO_2$ and CO with aerosol optical depth (AOD) and single-scattering albedo (SSA) from the NASA-TROPOMI aerosol algorithm (TropOMAER) product (Torres et al., 2020). AOD quantifies total light extinction, whereas SSA describes how that extinction is partitioned between scattering and absorption, allowing aerosol loading and absorptivity to be investigated simultaneously across large wildfire populations. This distinction is important because aerosol loading and aerosol absorptivity need not evolve identically during plume transport and therefore may provide complementary information on wildfire emissions and atmospheric processing. Combined with fire radiative power (FRP) and vapor pressure deficit (VPD), these observations are used to investigate how combustion conditions, fuel dryness, and land cover type influence wildfire aerosol optical properties. We first characterize the fire conditions and aerosol optical properties of the sampled wildfire plumes. We then investigate how combustion indicators derived from $NO_2$, CO, and FRP relate to aerosol loading and absorptivity across different land cover types. Finally, we use plume-core and box-size analyses to investigate how aerosol loading, aerosol absorptivity, and trace gas abundance vary spatially within individual wildfire plumes and what these spatial patterns reveal about early atmospheric processing.

## 2 Materials and methods

### 2.1 Fire locations

The analysis focuses on the Australian 2018–2019 and 2019–2020 fire seasons, which encompass wildfires across much of the continent. Australia and northern North America were initially identified as suitable study regions because both experienced frequent wildfires spanning a wide range of land cover types, with limited anthropogenic interference and high availability of TROPOMI observations. However, most North American wildfires did not exceed the CO threshold required for classification as biomass burning aerosol in the TropOMAER retrieval algorithm. Consequently, a different aerosol model was used to retrieve aerosol optical depth and single-scattering albedo from the measured radiances (Torres et al., 2013, 2020). To ensure consistent aerosol retrievals across the dataset, the present analysis is therefore restricted to the Australian 2018–2019 and 2019–2020 fire seasons.

### 2.2 TROPOMI data

The TROPOspheric Monitoring Instrument (TROPOMI) is a spectrometer on ESA's Copernicus Sentinel-5 Precursor (S-5P) satellite (Veefkind et al., 2012) that provides daily global coverage of trace gases relevant to air quality and climate. The spatial resolution of TROPOMI at nadir for the UV-visible wavelength range is 3.5 x 5.5 $km^2$ after 6 August 2019 and 3.5 x 7.0 $km^2$ before, and 7.0 x 5.5 $km^2$ after 6 August 2019 and 7.0 x 7.0 $km^2$ before for the shortwave-infrared wavelength. $NO_2$ is retrieved in the UV-visible wavelength range and CO in the shortwave-infrared wavelength range. AOD and SSA are reported at 388

https://doi.org/10.5194/egusphere-2026-5052
Preprint. Discussion started: 8 September 2026


nm. The S-5P satellite crosses the equator at 1:30 pm local solar time. Here we use operational data version 2 of reprocessed $NO_2$ tropospheric vertical column densities (van Geffen et al., 2022) and CO vertical column densities (Borsdorff et al., 2019; Landgraf et al., 2016), and version 1.1.1 AOD and SSA data based on the TropOMAER retrieval (Torres et al., 2013, 2020), from 1 September 2018 to 31 January 2019, and from 1 September 2019 to 31 January 2020. All TROPOMI orbit file data are gridded on a rectilinear latitude/longitude grid with a resolution of 0.05° x 0.05°, using the overlap of the satellite's ground pixel corners with the grid boxes to generate weighted averages. $NO_2$ and CO are filtered for a quality assurance value >= 0.5. AOD and SSA data are only used for data points labeled as smoke and selected with a final algorithm flag of 0, i.e., "best" data.

**2.3 Fire radiative power, land cover type, and meteorological data**

We used the collection 2 VIIRS 375 m active fire product from the Visible Infrared Imaging Radiometer Suite (VIIRS) instrument aboard the Suomi National Polar-orbiting Partnership (Suomi-NPP) satellite, accessed through NASA's Fire Information for Resource Management System (FIRMS) (Schroeder et al., 2014). FRP data were filtered to include daytime measurements, which are within minutes of TROPOMI measurements, and with a nominal or high confidence level. For analysis purposes, summed FRP data were also gridded to 0.05° x 0.05° latitude/longitude.

To classify land cover types, we used the Terra and Aqua satellites combined Moderate Resolution Imaging Spectroradiometer (MODIS) annual CMG V061 - MCD12C1 product (Friedl & Sulla-Menashe, 2022). This is a level 3 global data product on a spatial resolution of 0.05° x 0.05° latitude/longitude that matches the resolution of our gridded TROPOMI data. For land cover classification we use the Annual International Geosphere-Biosphere Programme (IGBP) land cover type encoding for the years 2018 through 2020. Our final analysis includes the following land cover types: grasslands, open shrublands, closed shrublands, woody savannas, savannas, and evergreen broadleaf forests. To improve data statistics, open and closed shrublands were combined as "shrublands" and woody savannas and savannas were combined into "savannas".

To characterize atmospheric fuel-drying conditions at the time of each wildfire observation, we calculated vapor pressure deficit (VPD). VPD is defined as the difference between the saturation and actual water vapor pressure and provides a measure of the atmosphere's evaporative demand (Seager et al., 2015). Because it is closely related to fuel moisture and wildfire activity, VPD is widely used as an indicator of fire weather and fire risk (Abatzoglou and Williams, 2016). Here, we calculated VPD for the TROPOMI overpass time on a 0.05° x 0.05° latitude/longitude grid using 2m air temperature and 2m dewpoint temperature data from the ERA-5 reanalysis from the European Centre for Medium-Range Weather Forecasts (Hersbach et al., 2020). ERA-5 data have an hourly temporal resolution and a spatial resolution of 0.25° x 0.25° latitude/longitude. All data are horizontally extrapolated to match the spatial resolution of the gridded satellite data and interpolated in time to match the satellite's overpass.

https://doi.org/10.5194/egusphere-2026-5052
Preprint. Discussion started: 8 September 2026


### 2.4 Analysis Framework and Metrics

To enable the analysis of a large ensemble of wildfire plumes, we developed an automated plume identification and characterization algorithm. The algorithm combines coincident TROPOMI trace gas and aerosol observations with FRP detections, VPD calculations, and land cover data. It then identifies and delineates wildfire plumes, derives plume and fire characteristics, applies quality criteria, and stores the resulting metrics for subsequent analysis. The complete processing workflow is summarized in Fig. 1, and the following sections describe each component in detail.

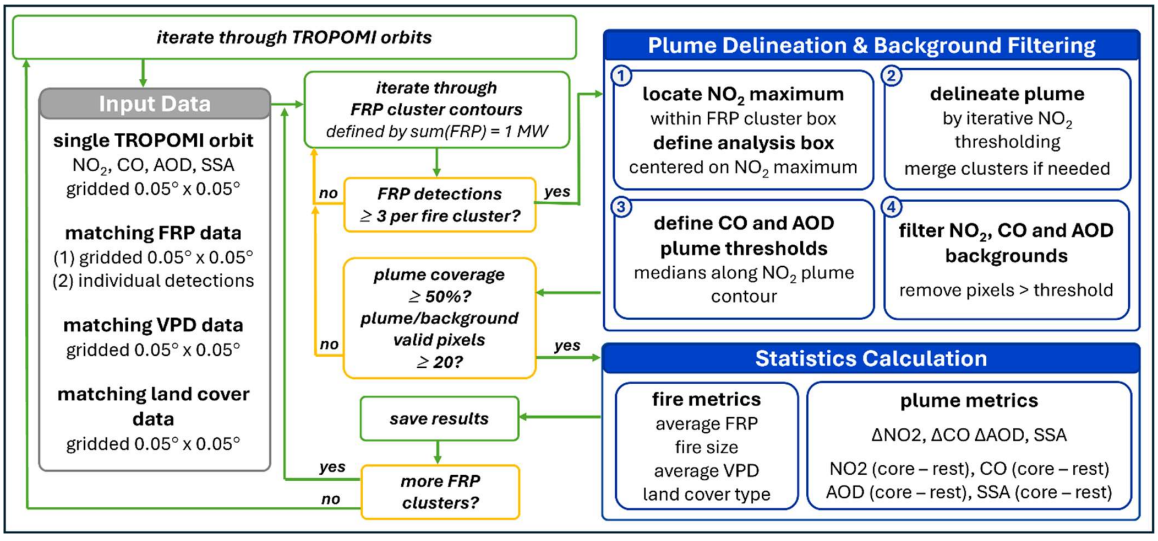


**Figure 1:** Flowchart of the automated plume identification and characterization algorithm.

For each TROPOMI orbit, FRP cluster contours were derived from the gridded FRP data using contour lines of summed FRP = 1 MW. Only FRP cluster contours containing at least three individual FRP detections were retained for further analysis. These thresholds were determined empirically and effectively excluded FRP clusters lacking significant $NO_2$ enhancements. For each retained FRP cluster contour, the location of the maximum $NO_2$ enhancement was identified within a rectangular FRP cluster box surrounding the contour and used as the center of a 0.8° x 0.8° latitude/longitude analysis box. Note that, although analysis box dimensions are reported throughout in degrees latitude and longitude, the longitudinal extent of each analysis box was adjusted according to the fire latitude to maintain approximately equal physical dimensions in both directions. Figure 2a shows an example of an identified FRP cluster contour and the corresponding $NO_2$ maximum within the FRP cluster box for a grassland fire on 6 December 2019. The wildfire plume perimeter was subsequently derived from the $NO_2$ enhancement field using an iterative thresholding approach. Starting from a high $NO_2$ threshold, the threshold was progressively lowered until the closed contour surrounding the $NO_2$ maximum either opened or merged with a neighboring

https://doi.org/10.5194/egusphere-2026-5052
Preprint. Discussion started: 8 September 2026


$NO_2$ enhancement. The final plume perimeter was defined as the last closed contour before either condition occurred, thereby minimizing contamination from nearby plumes while retaining the contiguous $NO_2$ enhancement associated with the target fire. Smaller FRP cluster contours contained within the plume perimeter that lacked a distinct associated plume were incorporated into the target plume. Figure 2 illustrates the resulting plume perimeter together with the corresponding $NO_2$, CO, AOD, and SSA fields.

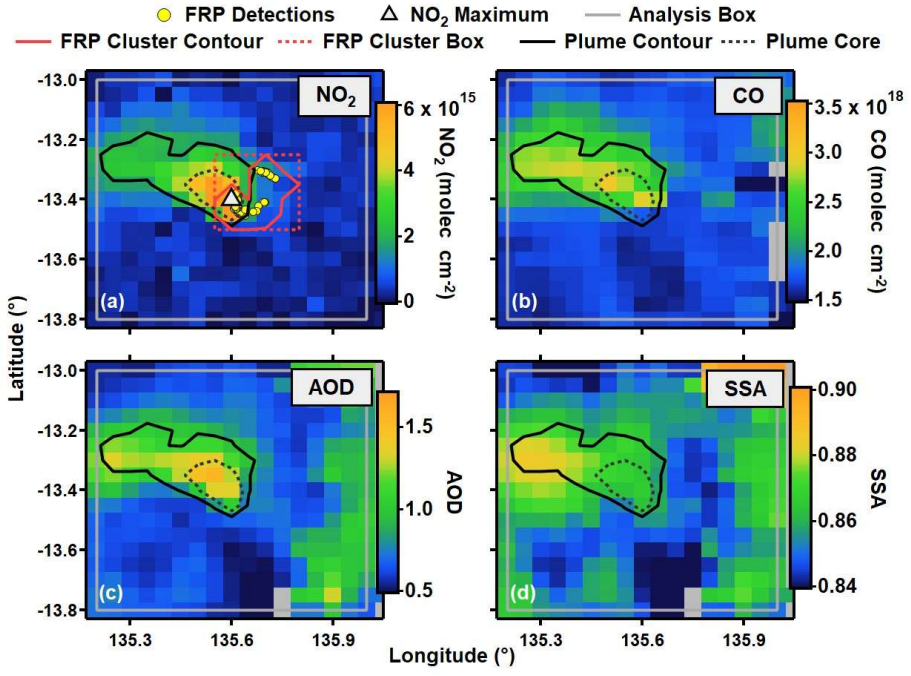


**Figure 2:** Example of a grasslands smoke plume detection on 6 December 2019 and corresponding (a) $NO_2$, (b) CO, (c) AOD, and (d) SSA TROPOMI observations. FRP detections, FRP cluster contour and associated $NO_2$ maximum within the FRP cluster box are included in panel (a). Black solid lines denote the $NO_2$-derived plume perimeter and black dashed lines indicate the regions defined as plume core. Each panel includes the 0.8° x 0.8° latitude/longitude analysis box that is centered on the $NO_2$ maximum.

Following plume delineation, local background values for $NO_2$, CO, and AOD were determined from pixels within the analysis box that were not associated with the identified plume. To reduce contamination from additional smoke plumes, pixels with $NO_2$ values exceeding the plume-defining $NO_2$ threshold were excluded from the background calculation. Because CO and aerosol particles have substantially longer atmospheric lifetimes than $NO_2$, the corresponding background thresholds were

https://doi.org/10.5194/egusphere-2026-5052
Preprint. Discussion started: 8 September 2026


derived from the median CO and AOD values along the $NO_2$ plume boundary and used to exclude residual smoke-affected pixels from the background estimates. For subsequent analysis, plumes were required to have at least 50% valid plume data coverage, and both the plume and background regions were required to contain a minimum of 20 valid data pixels.

For each retained plume, fire and plume statistics were calculated. Average FRP was derived from individual FRP detections within the FRP cluster contour. Fire size was quantified as the number of 0.05° x 0.05° latitude/longitude grid cells enclosed by the FRP cluster contour line, while average VPD was calculated as the mean value across those grid cells. Land cover type was assigned from these same grid cells and according to the dominant land cover fraction when multiple land cover types were present. Wildfire plume averages were calculated from pixels within the $NO_2$-defined plume perimeter. As a consistency check for plume SSA, we compared the arithmetic plume-averaged SSA with the corresponding AOD-weighted mean. The excellent agreement between the two ($R^2 = 0.99$) indicates that spatial variations in aerosol loading introduce negligible bias into the plume-averaged SSA used throughout this study. Plume column enhancements for $NO_2$, CO, and AOD, referred to as $\Delta NO_2$, $\Delta CO$, and $\Delta AOD$, were calculated by subtracting the corresponding local background from the plume-averaged total column. The trace gas column ratio $\Delta NO_2/\Delta CO$ was determined from the slope of a linear fit across plume and background pixels within the analysis box to minimize sensitivity to background offsets and provide a plume-scale measure of $NO_2$ enhancement relative to CO. To characterize plume structure, plumes were divided into "core" and "rest," where the plume core was defined as pixels exceeding the 80th percentile of plume $\Delta NO_2$. Plume dilution was approximated using the ratio of plume $\Delta CO$ to the 95th percentile of plume $\Delta CO$, with smaller values indicating greater dilution relative to the least diluted portions of the plume. Finally, fires located near major anthropogenic $NO_2$ sources were excluded by applying a threshold of $2.5 \times 10^{15}$ molecules $cm^{-2}$ to the long-term average $NO_2$ column derived from the complete analysis period.

Within the data set analyzed, we found 27730 FRP cluster contours with an associated $NO_2$ delineated smoke plume. Out of these plumes, 27531 passed the anthropogenic $NO_2$ filter, 7959 passed the quality filters for $NO_2$ and CO, and 1268 had available and sufficient aerosol data coverage. The following analysis is based on the 1268 plumes that passed all quality controls. An overview of the fire locations for these plumes is provided in Fig. S1, overlaid on both the original MODIS land cover map and the adapted land cover map used in this study.

### 2.5 Retrieval limitations and uncertainties

Potential biases in the operational TROPOMI $NO_2$ retrieval due to aerosol shielding warrant consideration when interpreting $\Delta NO_2/\Delta CO$. Dense smoke can reduce satellite sensitivity to $NO_2$, whereas the CO retrieval is substantially less sensitive to aerosol loading (Anderson et al., 2023; Rowe et al., 2022). Anderson et al. (2023), however, demonstrated that aerosol shielding primarily affects the absolute magnitude of retrieved $\Delta NO_2/\Delta CO$ ratios while preserving their dependence on combustion conditions. Consequently, aerosol shielding may influence the absolute values reported here but is unlikely to alter the relative differences among land cover types or the inferred relationships between combustion conditions and aerosol optical properties.

https://doi.org/10.5194/egusphere-2026-5052
Preprint. Discussion started: 8 September 2026


Additional uncertainties arise from assumptions embedded in the TropOMAER aerosol retrieval. Retrieved AOD and SSA depend on the assumed aerosol optical model, surface reflectance, and aerosol layer height (ALH). The retrieval employs an ALH climatology, while coincident Atmospheric Infrared Sounder (AIRS) total column CO observations are used to distinguish carbonaceous aerosols from other aerosol types (Torres et al., 2013, 2020). Because the sensitivity of near-UV radiances to absorbing aerosols increases with ALH (Torres et al., 2020), differences between the assumed climatological and actual ALH can introduce systematic biases in retrieved AOD and SSA. This is particularly relevant for wildfire smoke because plume injection height can depend on combustion conditions, implying that ALH-related retrieval biases may also vary systematically with combustion regime. Further, TropOMAER uses gridded AIRS total-column CO observations at 1° × 1° latitude/longitude resolution. Because AIRS CO is available only at regional scales, aerosol-type selection is informed by the broader atmospheric environment rather than local plume structure. Consequently, the assumed aerosol model may not always represent the actual aerosol composition within individual wildfire plumes or their surrounding background, particularly where aerosol properties vary over spatial scales smaller than the AIRS footprint.

Since plume aerosol enhancements here are obtained by subtracting local background AOD from the total-column retrieval, uncertainties in the retrieved background aerosol directly affect the magnitude of ΔAOD. To better understand elevated background AOD values, we inspected representative cases using coincident true color satellite imagery. While some cases exhibited widespread regional haze and smoke consistent with elevated background aerosols, several shrubland, grassland, and savanna cases showed moderately elevated background AOD (typically exceeding 0.3) despite little or no visible evidence of smoke. These latter cases were also generally not accompanied by obvious enhancements in background CO relative to the surrounding regional field, although the true non-smoke CO background is difficult to establish because of substantial spatial variability and frequent smoke influence across Australia. Together, these observations suggest that elevated background AOD in a subset of cases may reflect limitations associated with regional aerosol type selection, assumed ALH, surface reflectance, or combinations thereof. Retrieval-related sensitivities may also lead to missing observations near active fire fronts, thereby reducing the sampling of the youngest and most concentrated smoke.

These retrieval limitations primarily affect analyses that depend directly on AOD, such as comparisons of plume aerosol loading among land cover types and box-size analyses. In contrast, analyses based on relative spatial variability within individual plumes are expected to be substantially less sensitive because they rely on coincident retrievals within the same retrieval scene. Because this study focuses on individual wildfire plumes rather than long-term climatological aerosol distributions, departures from the climatological aerosol assumptions employed by the retrieval may be particularly important. The potential influence of these retrieval limitations is considered where relevant in the interpretation of the results.

https://doi.org/10.5194/egusphere-2026-5052
Preprint. Discussion started: 8 September 2026


## 3 Results and discussion

### 3.1 Characteristics of fire conditions and aerosol optical properties

The fires included in this analysis span a broad range of burning conditions and aerosol optical properties. Figure 3 summarizes the distributions of average FRP, fire size, VPD, $\Delta NO_2/\Delta CO$, $\Delta AOD$, and SSA for all sampled wildfires, separated by land cover type. The distributions of average FRP (Fig. 3a) are characterized by long upper tails across all land cover types, indicating that a relatively small number of fires account for the highest FRP values, as reflected by mean values that consistently exceed the corresponding medians. Grasslands, savannas, and evergreen broadleaf forests exhibit similar FRP distributions, whereas shrublands are characterized by the highest mean and median FRP values (25 MW and 21 MW, respectively). Fire size distributions (Fig. 3b) are strongly weighted toward smaller fires. Mean and median fire sizes are comparable among all four land cover types and range between five and nine grid cells. VPD distributions (Fig. 3c) are approximately symmetric but differ substantially in magnitude. Shrublands burn under the driest conditions, with a mean VPD of 58 hPa, followed by grasslands, savannas, and evergreen broadleaf forests.

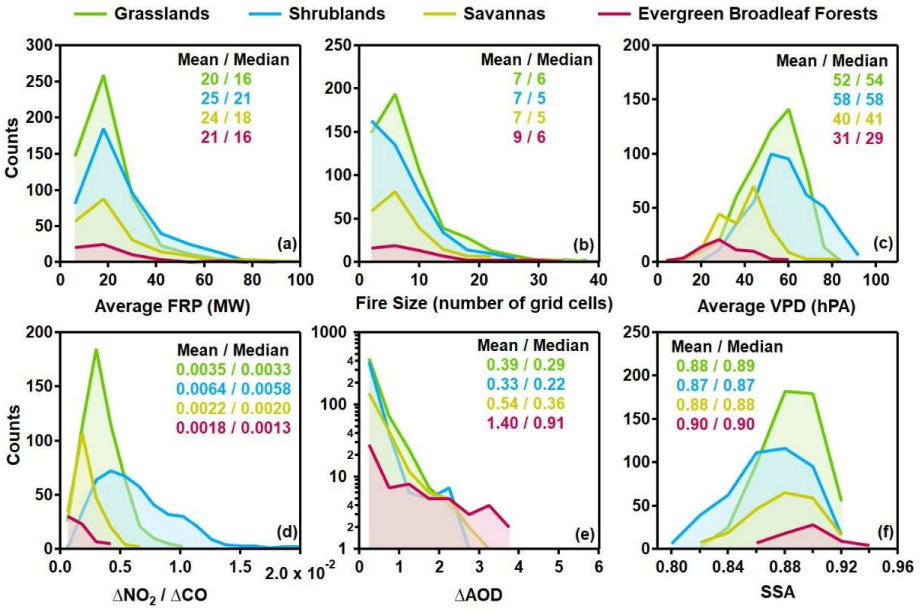


**Figure 3:** Histograms of (a) average FRP, (b) fire size, (c) average VPD, (d) $\Delta NO_2/\Delta CO$, (e) $\Delta AOD$, and (f) SSA. Note the logarithmic y-axes in panel (e).

https://doi.org/10.5194/egusphere-2026-5052
Preprint. Discussion started: 8 September 2026


The $\Delta NO_2/\Delta CO$ distributions (Fig. 3d), which serve as a proxy for the relative contributions of flaming and smoldering combustion, exhibit a similar ordering. Shrublands show the highest mean $\Delta NO_2/\Delta CO$ of 0.0064, indicating the greatest contribution from flaming combustion, whereas evergreen broadleaf forests are characterized by more smoldering combustion with a mean $\Delta NO_2/\Delta CO$ of 0.0018, indicating substantial differences in combustion behavior among the land cover types. These findings are in line with previous TROPOMI observations by van der Velde et al. (2021), who found that savanna fires exhibit higher $\Delta NO_2/\Delta CO$ ratios reflecting a larger contribution from flaming combustion compared to temperate forest fires that were characterized by lower $\Delta NO_2/\Delta CO$ values and stronger smoldering signatures. While fuel nitrogen content can also influence $\Delta NO_2/\Delta CO$, the ratio is used here primarily as an indicator of combustion conditions. Although aerosol shielding may reduce the absolute magnitude of retrieved $\Delta NO_2/\Delta CO$ under conditions of dense smoke (Section 2.5), previous work has shown that it largely preserves the relative dependence of $\Delta NO_2/\Delta CO$ on combustion conditions (Anderson et al., 2023). Consequently, aerosol shielding is unlikely to explain the systematic differences in $\Delta NO_2/\Delta CO$ observed among the four land cover types. All land cover types display distributions skewed toward lower $\Delta NO_2/\Delta CO$ values, although the shrubland distribution is more symmetric. The predominance of lower $\Delta NO_2/\Delta CO$ values is consistent with the expectation that strongly flaming combustion often represents a shorter phase of the burning process, whereas smoldering combustion can persist for longer periods (Akagi et al., 2011; Andreae, 2019). This behavior is also consistent with satellite observations of wildfire $\Delta NO_2/\Delta CO$ over time reported by Anderson et al. (2023). Because satellite observations provide only intermittent snapshots of fire activity, the probability of sampling these highly flaming conditions is relatively low. As a result, most observations represent more mature combustion states with lower $\Delta NO_2/\Delta CO$ values, leading to distributions weighted toward less flaming-dominated combustion.

Figure 3e and f show the distributions of plume-averaged and background-corrected AOD, ΔAOD, and plume-averaged SSA. For all land cover types, the ΔAOD distributions are strongly skewed toward lower values and decrease approximately exponentially toward higher ΔAOD. Mean ΔAOD values for grasslands, shrublands, and savannas range from 0.33 to 0.54, whereas evergreen broadleaf forests exhibit substantially larger optical depths with a mean ΔAOD of 1.4 and a more pronounced high-AOD tail. In contrast, SSA distributions are comparatively symmetric across all land cover types, but systematic differences are evident. Shrublands are shifted toward lower SSA values, indicating aerosols that are more absorbing, whereas evergreen broadleaf forests are shifted toward higher SSA values, consistent with more scattering-dominated particles. Although combustion conditions likely explain most of the observed SSA differences, systematic ALH-related retrieval sensitivities may also contribute.

Collectively, these distributions suggest that drier fuels and larger flaming fractions tend to produce more absorbing aerosol populations and lower SSA values, whereas land cover types characterized by lower flaming fractions and larger fire sizes tend to exhibit larger AODs. As discussed in Section 2.5, uncertainties in retrieved background AOD primarily affect ΔAOD and are expected to be greatest over shrubland, grassland, and savanna regions, where elevated background AOD may partly reflect retrieval assumptions rather than biomass burning aerosol alone. In contrast, the substantially larger ΔAOD observed for evergreen broadleaf forests is consistent with widespread regional smoke apparent in coincident true-color imagery.

https://doi.org/10.5194/egusphere-2026-5052
Preprint. Discussion started: 8 September 2026


Because ΔAOD represents only the enhancement above the local background, and accounts for only about half of the corresponding total-column AOD on average (Fig. S2), it should be interpreted as a measure of plume aerosol enhancement rather than absolute plume aerosol loading.

### 3.2 Effects of fire and combustion conditions on aerosol optical properties

To investigate the factors controlling aerosol optical properties across fires in different land cover types, we first examined relationships among the fire and combustion metrics used to characterize burning conditions and then assessed how these metrics relate to AOD and SSA. Results are presented in Figs. 4 and 5, which show binned medians and interquartile ranges for all variables. Marker sizes represent a third variable as indicated in the figure captions. Note that, because each bin was required to contain at least six data points, not all data points shown in Fig. 3 are included in the subsequent analyses.

Figure 4 characterizes relationships among fire intensity, fuel dryness, and combustion indicators. Panel (a) shows the relationship between $\Delta NO_2/\Delta CO$ and average FRP, with marker size scaled to fire size. For all land cover types, $\Delta NO_2/\Delta CO$ increases with FRP at low to moderate fire intensity, indicating a larger fraction of flaming combustion as fire radiative output increases. The relationship is strongest below approximately 30 to 40 MW, where increases in FRP are accompanied by increases in both $\Delta NO_2/\Delta CO$ and fire size. At higher FRP, however, the dependence weakens and in some cases levels off. This behavior may reflect limitations on fire spread at high intensity, including reduced fuel continuity and landscape fragmentation. Similar nonlinear relationships between FRP and fire size have been reported previously for many fire-prone ecosystems, where fire size increases with FRP only up to intermediate fire intensities before reaching a threshold (Laurent et al., 2019). Anderson et al. (2023) likewise observed a positive relationship between $\Delta NO_2/\Delta CO$ and FRP, consistent with greater relative $NO_2$ emissions during more intense, flaming-dominated combustion.

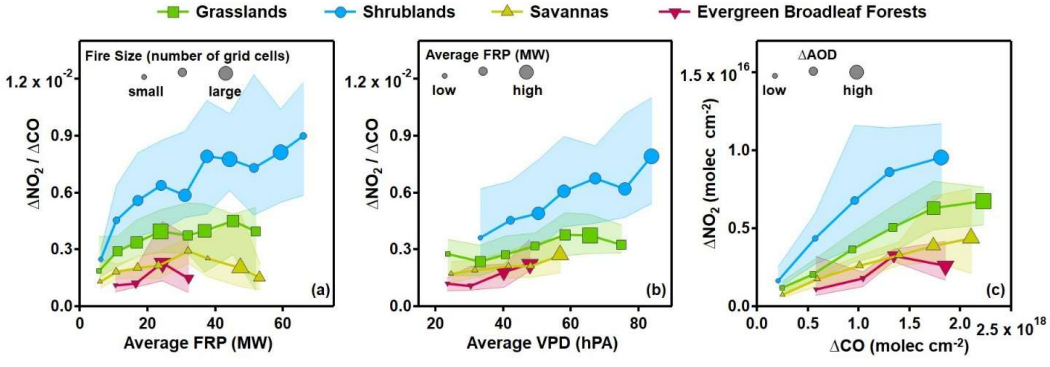


**Figure 4:** Relationships among fire intensity, fuel dryness, and combustion indicators for the four land cover types. (a) $\Delta NO_2/\Delta CO$ vs average FRP, (b) $\Delta NO_2/\Delta CO$ vs average VPD, and (c) $\Delta NO_2$ vs $\Delta CO$. Points denote binned median values and

https://doi.org/10.5194/egusphere-2026-5052
Preprint. Discussion started: 8 September 2026


shading indicates the 25th–75th percentile range. Marker sizes represent median (a) fire size, (b) FRP, and (c) ΔAOD. Marker sizes are normalized separately for each land cover type.

The relationship between $\Delta NO_2/\Delta CO$ and average VPD is shown in Fig. 4b. All land cover types exhibit generally increasing $\Delta NO_2/\Delta CO$ with increasing VPD, indicating that drier environmental conditions favor a larger fraction of flaming combustion. Variations in marker size reveal a concurrent increase in FRP, suggesting that combustion intensity, fuel dryness, and combustion phase are closely linked. Together, panels (a) and (b) demonstrate that overall $\Delta NO_2/\Delta CO$ is a useful indicator of the relative balance between flaming and smoldering combustion, although the relationship is modulated by fire size, fuel availability, and environmental conditions.

Figure 4c shows the relationship between plume-averaged and background-corrected $NO_2$ and CO column enhancements. Across all land cover types, $\Delta NO_2$ increases with ΔCO, indicating that larger trace gas enhancements are generally associated with stronger wildfire emissions. However, the relationship differs systematically among fuel types. Shrubland fires exhibit the steepest increase in $\Delta NO_2$ with increasing ΔCO, whereas evergreen broadleaf forest fires show the weakest increase. These differences suggest systematic variations in combustion characteristics among fuel types, consistent with the $\Delta NO_2/\Delta CO$ distributions discussed above (Fig. 3d). Marker sizes scaled to ΔAOD generally increase with ΔCO, reflecting larger aerosol burdens associated with stronger emissions. Scaling marker sizes to total column AOD produces nearly identical patterns, indicating that the inferred relationship between combustion characteristics and trace gas enhancements is insensitive to the choice of plume-averaged AOD definition.

Figure 5 examines how fire and combustion metrics relate to aerosol optical properties. In panel (a), ΔAOD is plotted vs ΔCO. Across all land cover types, ΔAOD generally increases with ΔCO, while marker sizes proportional to fire size likewise tend to increase toward larger ΔAOD values, indicating that AOD is strongly linked to total emissions and fuel consumption. The observed increase of ΔAOD with ΔCO is consistent with the close association between emissions of CO and organic aerosol in wildfire smoke. Because organic aerosols typically constitute most of the aerosol mass in wildfire plumes and are efficient light scatterers, they often dominate total aerosol extinction and therefore contribute strongly to AOD (Akagi et al., 2011; Andreae, 2019; Reid et al., 2005b). Figure 5b shows the dependence of ΔAOD on fire size. For all land cover types, larger fires are associated with higher AOD, although substantial variability is present for a given fire size. Marker sizes scaled by ΔCO demonstrate that increases in ΔAOD are accompanied by larger trace gas enhancements, reinforcing the interpretation that aerosol loading is primarily governed by total emissions. Evergreen broadleaf forests stand out from the other land cover types by producing substantially larger ΔAOD and ΔCO values for comparable fire sizes. This behavior is consistent with the larger fuel loads and generally less dry conditions characteristic of forest ecosystems, which support comparatively greater emissions of both aerosol and trace gases per unit area burned. Figure 5c examines the relationship between ΔAOD and $\Delta NO_2/\Delta CO$. No clear monotonic relationship is observed for any land cover type, indicating that combustion phase is not the dominant control on aerosol loading in this ensemble. Evergreen broadleaf forests exhibit the largest spread in ΔAOD, particularly at low $\Delta NO_2/\Delta CO$ values, suggesting that smoldering-dominated combustion can generate large aerosol burdens

https://doi.org/10.5194/egusphere-2026-5052
Preprint. Discussion started: 8 September 2026


when sufficient fuel is available. Anderson et al. (2023) reported a positive relationship between AOD and $\Delta NO_2/\Delta CO$ for an individual wildfire event, where changes in AOD primarily reflected the evolution of the same fire over time. In contrast, each $\Delta NO_2/\Delta CO$ bin in the present analysis contains many different fires spanning a wide range of fire sizes, fuel loads, and total emissions. Consequently, variability in total emissions dominates the AOD distribution within each combustion-regime bin, masking the underlying dependence on combustion phase. To assess the sensitivity of these relationships to the AOD background correction, the analyses shown in Fig. 5a, b, and c were repeated using total column AOD in place of ΔAOD (Fig. S3). The resulting relationships are nearly identical, indicating that the observed dependence of plume aerosol loading on ΔCO, fire size, and $\Delta NO_2/\Delta CO$ is robust to the treatment of the background aerosol.

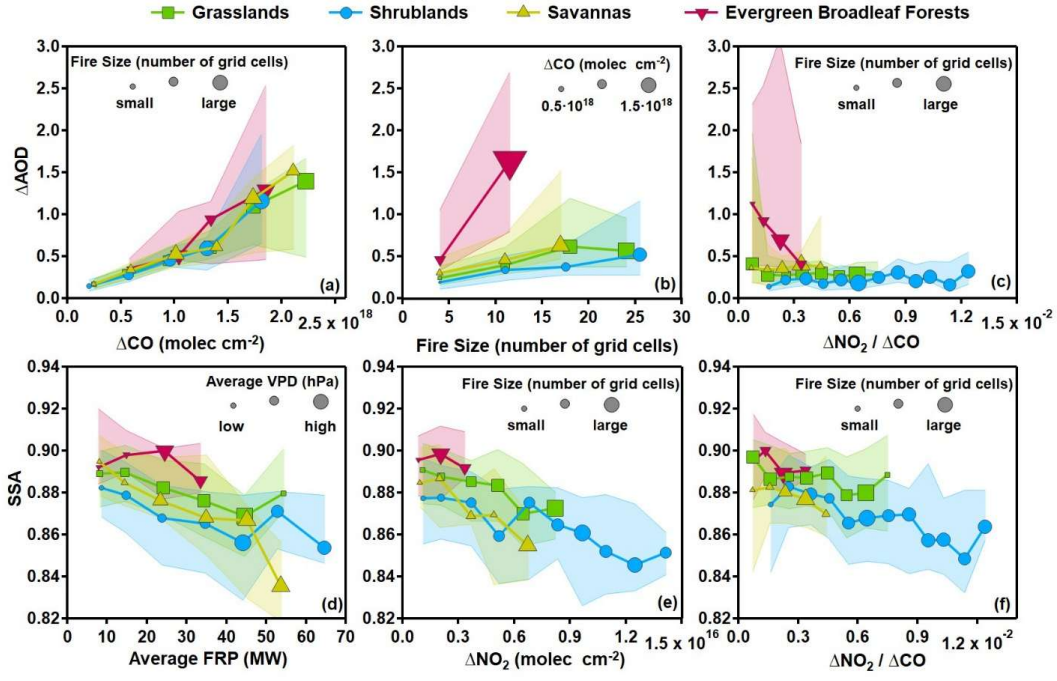


**Figure 5:** Relationships between fire and combustion metrics and aerosol optical properties for the four land cover types. AOD is plotted vs (a) ΔCO, (b) fire size, (c) $\Delta NO_2/\Delta CO$. SSA is plotted vs (d) average FRP, (e) $\Delta NO_2$, and (f) $\Delta NO_2/\Delta CO$. Points denote binned median values and shading indicates the 25th–75th percentile range. Marker sizes represent fire size in panels (a), (c), (e), and (f), ΔCO in panel (b), and average VPD in panel (d). Marker sizes are normalized separately for each land cover type, or as labeled.

https://doi.org/10.5194/egusphere-2026-5052
Preprint. Discussion started: 8 September 2026


Figure 5d, e, and f show relationships between SSA and average FRP, $\Delta NO_2$, and $\Delta NO_2/\Delta CO$, respectively. Across all land cover types, SSA decreases with increasing FRP, increasing $\Delta NO_2$, and increasing $\Delta NO_2/\Delta CO$. These correlations indicate that aerosols emitted from more intense fires that burn under larger fractions of flaming combustion, and that are characterized by higher $NO_x$ emissions are systematically more absorbing. The similarity of the trends across FRP, $\Delta NO_2$, and $\Delta NO_2/\Delta CO$ reflects the close coupling between fire intensity and combustion phase identified in Fig. 4. Variations in fuel dryness indicated by marker size scaled to average VPD in panel (d) and variations in fuel load indicated by marker size scaled to fire size in panels (e) and (f), as well as large quartile ranges demonstrate that these factors are not independent but evolve together. The observed decreases in SSA under increasingly flaming conditions are consistent with enhanced emissions of BC relative to OC aerosol. Flaming combustion favors the production of highly absorbing BC, whereas smoldering combustion produces larger quantities of organic aerosol that contribute primarily to scattering. Consequently, shifts toward more flaming combustion reduce SSA by increasing the relative contribution of aerosol absorption. Although retrieved SSA may also be influenced by systematic retrieval sensitivities (Section 2.5), the consistent relationships between SSA across multiple combustion metrics indicate that combustion conditions exert a first-order control on aerosol absorptivity across all land cover types examined in this study. Taken together, these results reveal distinct combustion and aerosol optical regimes across the four land cover types, which are summarized in Table 1. The land cover type ordering emphasizes the contrast between shrubland and evergreen broadleaf forest fires, which define the extremes of the observed relationships among fuel dryness, combustion phase, aerosol loading, and aerosol absorptivity.

**Table 1** Summary of fire metrics, combustion conditions, and aerosol optical properties for all land cover types.

| Metric | Shrublands | Evergreen Broadleaf Forests | Grasslands | Savannas |
|---|---|---|---|---|
| **FRP** | highest | lowest | intermediate | intermediate |
| **VPD** | highest | lowest | high | intermediate |
| **Fire Size** | smallest | largest | intermediate | intermediate |
| **$\Delta NO_2/\Delta CO$** | highest | lowest | intermediate | intermediate |
| **Combustion Phase** | flaming-dominated | smoldering-dominated | mixed | mixed |
| **AOD** | lowest | highest | intermediate | intermediate |
| **SSA** | lowest | highest | intermediate | intermediate |

### 3.3 Spatial organization of aerosol optical properties

The relationships presented in Section 3.2 describe how combustion conditions influence plume-averaged aerosol optical properties across different land cover types. However, wildfire plumes are spatially heterogeneous, with substantial variability in aerosol and trace gas concentrations occurring within individual plumes. To characterize this spatial variability, we employed two complementary analyses. The first compares $NO_2$-defined plume cores, representing the most combustion-

https://doi.org/10.5194/egusphere-2026-5052
Preprint. Discussion started: 8 September 2026


influenced regions of the plume, with the surrounding plume ("rest"), thereby quantifying spatial gradients in aerosol loading and absorptivity. The second examined how plume-averaged aerosol optical properties vary with increasing analysis-box size, providing complementary information on the spatial organization of aerosol optical properties across progressively larger portions of wildfire plumes.

Figure 6a and b show the core-rest analysis by relating AOD (core-rest) and SSA (core-rest), respectively, to CO (core-rest), with marker size representing $NO_2$ (core-rest). Positive values indicate higher concentrations in the $NO_2$-defined plume core than in the surrounding plume. Distributions of plume core-rest differences for $NO_2$, CO, AOD, and SSA are provided in Fig. S4. All land cover types exhibit positive core-rest differences in both AOD and CO (Fig. 6a), showing that $NO_2$-defined plume cores are characterized by enhanced aerosol loading and trace gas abundance. Furthermore, AOD (core-rest) increases with CO (core-rest) across all land cover types, indicating that spatial gradients in aerosol loading closely follow those in the relatively long-lived tracer CO. Larger $NO_2$ (core-rest) enhancements generally coincide with larger CO (core-rest) values despite the more rapid chemical loss of $NO_2$.

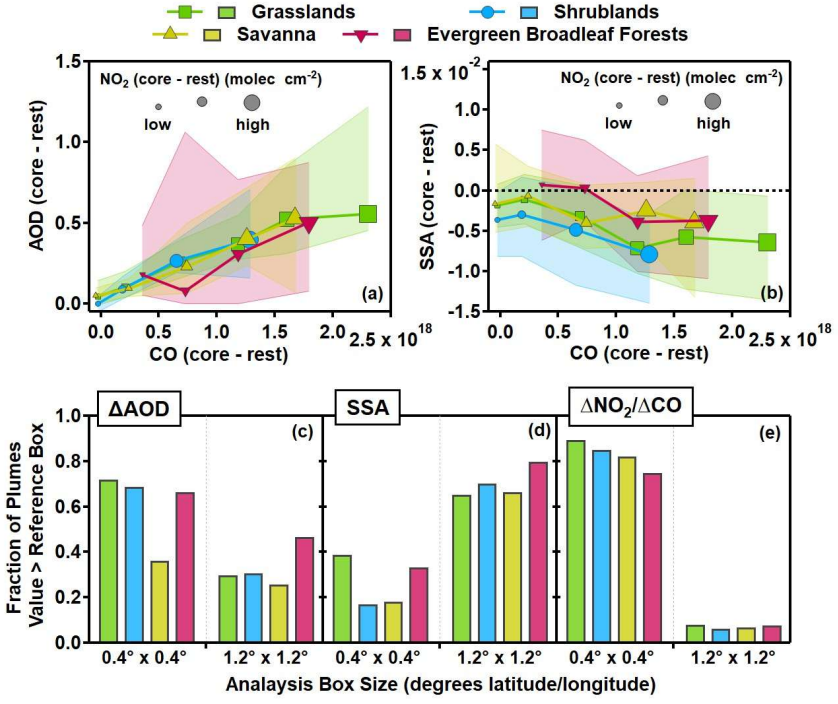


**Figure 6**: Spatial organization of aerosol optical properties within wildfire plumes for the four land types. (a) Core-rest differences in AOD and (b) SSA as a function of CO. Points denote binned median values and shading indicates the 25th–75th percentile range. Marker size represents the corresponding core-rest $NO_2$ difference and is normalized separately for each land

https://doi.org/10.5194/egusphere-2026-5052
Preprint. Discussion started: 8 September 2026


cover type. Panels (c–e) show the fraction of plumes for which ΔAOD, SSA, and $\Delta NO_2/\Delta CO$, respectively, exceed the corresponding value obtained using the reference 0.8° x 0.8° latitude/longitude analysis box when applying either a smaller (0.4° x 0.4°) or larger (1.2° x 1.2°) analysis box.

Figure 6b shows SSA (core-rest) as a function of CO (core-rest). In contrast to AOD, SSA (core-rest) remains close to zero across the full range of CO (core-rest), indicating that aerosol absorptivity exhibits substantially weaker spatial gradients than aerosol loading. Nevertheless, most observations exhibit slightly negative SSA (core-rest) values, indicating that plume cores are, on average, marginally more absorbing than surrounding plume regions. The core-rest analysis is insensitive to the choice of $NO_2$ percentile used to define the plume core, with 70th and 90th percentile thresholds producing qualitatively similar contrasts in AOD, SSA, CO, and $NO_2$ to those obtained using the 80th percentile threshold adopted in the main analysis.

The second analysis examines how plume-averaged aerosol optical properties vary with spatial scale by comparing results obtained using smaller (0.4° x 0.4° latitude/longitude) and larger (1.2° x 1.2° latitude/longitude) analysis boxes with those from the reference 0.8° x 0.8° analysis box. ΔAOD (Fig. 6c) decreases modestly with increasing analysis-box size across all land cover types, consistent with increasing dilution as progressively larger plume regions are sampled. The corresponding total column AOD exhibits the same qualitative box-size dependence across all land cover types (Fig. S5), indicating that the inferred dilution signal is robust to the treatment of the background aerosol. SSA plume averages shown in Fig. 6d reveal a systematic tendency toward increasing SSA with increasing spatial scale: between 61% and 83% of plumes exhibit lower SSA in the 0.4° x 0.4° analysis box than in the reference box, whereas between 65% and 80% exhibit higher SSA in the 1.2° x 1.2° box. Although retrieved SSA may also be influenced by systematic retrieval sensitivities (Section 2.5), these effects are unlikely to explain the consistent increase in SSA observed across multiple land cover types and analysis-box sizes. To distinguish dilution from concurrent chemical processing, Fig. 6e shows the corresponding behavior of $\Delta NO_2/\Delta CO$. The large majority of plumes exhibit distinctly higher $\Delta NO_2/\Delta CO$ in the smaller analysis box and lower values in the larger box. Previous work using the same type of box-size analysis demonstrated that this systematic decrease in $\Delta NO_2/\Delta CO$ results from the more rapid chemical loss of $NO_2$ relative to the much longer-lived CO (Anderson et al., 2023).

Although the two analyses examine plume structure from different perspectives, they arrive at a consistent conclusion. The core-rest analysis demonstrates that plume cores contain substantially higher aerosol loading but only slightly lower SSA than surrounding plume regions, while the box-size analysis shows that SSA increases as progressively larger portions of the plume are sampled. Together with the concurrent decrease in $\Delta NO_2/\Delta CO$, these observations indicate that aerosol absorptivity evolves while chemical processing is taking place. Consequently, the observed increase in SSA cannot be attributed to dilution alone but instead likely reflects the combined effects of chemical processing, dilution, and mixing. Note also that aerosol retrieval gaps near fire sources may underrepresent the youngest plume segments and some of the most rapid early changes in aerosol absorptivity. The agreement between the independent core-rest and box-size analyses provides confidence that the observed behavior in AOD and SSA is a robust characteristic of the sampled wildfire plumes, although the present observations cannot distinguish the relative contributions of individual processes altering the smoke plume.

https://doi.org/10.5194/egusphere-2026-5052
Preprint. Discussion started: 8 September 2026


The box-size dependence of AOD, SSA and $\Delta NO_2/\Delta CO$ reflects the spatial scales sampled by our analysis. Using a 0.8° x 0.8° latitude/longitude analysis box (approximately 90 km x 90 km at 10° S and 90 km x 70 km at 40° S) means that most observations represent plume ages of several hours rather than freshly emitted or multi-day transported smoke. Because the active fire is located near the center of each analysis box and TROPOMI observes each plume once daily around midday, this sampling primarily captures sub-daily plume evolution. Previous aircraft campaigns have documented rapid chemical transformation of wildfire smoke over these sub-daily timescales, with observations spanning fresh emissions to smoke several hours downwind (Kleinman et al., 2020; Warneke et al., 2023). The spatial gradients in aerosol and trace gas abundance observed here are consistent with plumes that have undergone substantial atmospheric processing while retaining distinct plume-core structure. Histograms of the CO dilution metric (see Section 2.4) yield remarkably similar distributions across all land cover types, with mean and median values near 0.5 (Fig. S6). These values indicate moderately diluted yet still well-defined smoke plumes, suggesting that substantial dilution has already occurred while distinct plume-core enhancements remain. Because the CO dilution metric quantifies the contrast between average plume conditions and the plume core, similar values across land cover types suggest that TROPOMI is sampling plumes in broadly comparable mixing states despite large differences in fire size, emissions, and plume aerosol loading.

## 4 Summary and conclusions

This study demonstrates that combustion conditions exert a first-order control on wildfire aerosol optical properties. More flaming combustion generally produces more absorbing aerosol populations, whereas more smoldering combustion is associated with larger AODs and more scattering-dominated smoke. The contrast is particularly evident between shrubland fires, which had the highest mean $\Delta NO_2/\Delta CO$ (0.0064), and evergreen broadleaf forest fires, which had the lowest (0.0018), with corresponding shifts from more absorbing toward more scattering aerosol populations. Across all land cover types analyzed here, consistent relationships between SSA, FRP, $\Delta NO_2$, and $\Delta NO_2/\Delta CO$ indicate that aerosol absorptivity responds systematically to variations in combustion phase and fire intensity, while $\Delta AOD$ is more strongly linked to total emissions and fuel loading, as reflected by its relationships with fire size and $\Delta CO$. Together, these results demonstrate that plume-averaged AOD and SSA observations provide complementary information about wildfire behavior, with AOD primarily reflecting emission strength and aerosol loading, and SSA primarily reflecting combustion conditions. These relationships were found to be largely insensitive to the choice of background-subtracted or total column AOD, providing confidence that the principal conclusions are not driven by the treatment of the background aerosol.

These findings are consistent with previous satellite observations linking higher $\Delta NO_2/\Delta CO$ to more flaming combustion across land cover types and to increasing fire radiative outpu (van der Velde et al., 2021; Anderson et al., 2023). However, whereas Anderson et al. (2023) observed increasing AOD with $\Delta NO_2/\Delta CO$ during the evolution of an individual fire, no clear monotonic relationship was found across the large fire ensemble analyzed here. This difference indicates that, across diverse wildfires, variability in total emissions and fuel loading can dominate aerosol loading and obscure its dependence on

https://doi.org/10.5194/egusphere-2026-5052
Preprint. Discussion started: 8 September 2026


combustion phase. The present results therefore extend previous trace-gas-based characterization of wildfire combustion by demonstrating that aerosol loading and absorptivity provide distinct and complementary information about wildfire emissions and combustion conditions.

The plume-core and box-size analyses demonstrate that atmospheric processing, dilution, and mixing collectively contribute to the observed spatial variability in aerosol loading and absorptivity and that AOD and SSA exhibit fundamentally different spatial behavior within wildfire plumes. Aerosol loading remains closely coupled with smoke abundance and dilution, whereas aerosol absorptivity exhibits substantially weaker spatial variability. Nevertheless, SSA changes systematically with spatial scale: 61-83% of plumes exhibited lower SSA in the 0.4° x 0.4° analysis box than in the 0.8° x 0.8° reference box, whereas 65-80% exhibited higher SSA in the 1.2° x 1.2° box. The accompanying decrease in $\Delta NO_2/\Delta CO$ with increasing analysis box size indicates that the observed increase in SSA occurs while chemical processing is simultaneously taking place, indicating that the spatial patterns are unlikely to reflect dilution alone. This behavior is consistent with previous aircraft observations showing rapid chemical transformation of wildfire smoke over timescales of several hours (Kleinman et al., 2020; Warneke et al., 2023). However, the present observations cannot distinguish the relative contributions of chemical processing, dilution, and mixing with surrounding aerosols. More broadly, these results indicate that aerosol absorptivity is more spatially homogeneous than aerosol loading and trace gas abundance over the plume scales sampled here. The consistency of plume-core and box-size analyses provides additional confidence that these inferred spatial patterns reflect plume evolution rather than methodological artifacts.

The relationships presented here provide observational constraints on the links between combustion conditions, aerosol optical properties, and the spatial organization of wildfire smoke, offering a framework for evaluating whether models realistically represent the coupled effects of emissions, aerosol growth, mixing, and chemical processing on aerosol radiative properties. More broadly, these observations add to the established understanding that wildfire aerosol optical properties are shaped by both combustion conditions and atmospheric processing by showing that aerosol loading and absorptivity exhibit distinct spatial behavior within wildfire plumes. Because the analysis is primarily sensitive to plume structure and atmospheric processing on sub-daily timescales, it does not directly constrain longer-timescale processes associated with multi-day transport, cloud processing, or changes in aerosol composition such as brown carbon photobleaching. Nevertheless, the results suggest that important changes in aerosol absorptivity occur on sub-daily timescales, highlighting the importance of accurately representing the coupled effects of combustion conditions, early plume mixing, and atmospheric processing when quantifying the radiative effects of wildfire aerosol in regional and global atmospheric models. The present analysis is also subject to retrieval uncertainties, however, the principal relationships between combustion conditions, aerosol optical properties, and plume structure were robust across the sensitivity analyses performed here.

Future work could combine TROPOMI aerosol observations with geostationary fire measurements, plume transport analyses, and meteorological data to investigate how diurnal variations in fire intensity and combustion conditions influence aerosol optical properties throughout the wildfire lifecycle. Such analyses could help link the statistical relationships identified here

https://doi.org/10.5194/egusphere-2026-5052
Preprint. Discussion started: 8 September 2026


between fire and combustion metrics and AOD and SSA to the temporal evolution of individual wildfire plumes, while providing additional constraints on the relative roles of emissions, atmospheric processing, dilution, and plume mixing.

**Code and data availability**

All data used in this study are publicly available. TROPOMI $NO_2$ (https://doi.org/10.5270/S5P-9bnp8q8) and CO (https://doi.org/10.5270/S5P-bj3nry0) data can be downloaded at https://browser.dataspace.copernicus.eu (last access: August 2026). TROPOMI aerosol data are available at https://daac.gsfc.nasa.gov (last access: August 2026). FRP data are available at https://firms.modaps.eosdis.nasa.gov/download (last access: August 2026). MODIS land cover data can be downloaded at https://www.earthdata.nasa.gov/data/catalog/lpcloud-mcd12c1-061 (last access: August 2026). ERA5 hourly data on single levels from 1940 to present can be found at https://cds.climate.copernicus.eu/datasets (last access: August 2026). The Igor Pro code used for automated wildfire smoke plume analysis and the resulting processed data underlying all figures in the main text are archived on Zenodo (Dix, 2026, https://doi.org/10.5281/zenodo.22036261). The corresponding development repository is available on GitHub (https://github.com/barbarakdix1200/Smoke-Plume-Processing).

**Author contributions**

BD and JdG designed the study. Funding acquisition was led by JdG. Formal analysis was conducted by BD with inputs from all co-authors. BD prepared the manuscript. All co-authors reviewed and edited the manuscript.

**Competing interests**

The authors declare that they have no conflict of interest.

**Acknowledgements**

This study uses data from the Copernicus Sentinel-5 Precursor mission, implemented by the European Space Agency (ESA) on behalf of the European Commission (EC). The contributions of BD, LDA, and JdG were supported by the NOAA AC4 program under grant number NA22OAR4310538. The contribution of LDA was further supported by the NSF GRFP program under grant number DGE 2040434. The contribution of JPV to this work was supported by the Netherlands Space Agency under the TROPOMI Science Contract. ChatGPT was used to improve language.

https://doi.org/10.5194/egusphere-2026-5052
Preprint. Discussion started: 8 September 2026


## References

Abatzoglou, J. T. and Williams, A. P.: Impact of anthropogenic climate change on wildfire across western US forests, Proc. Natl. Acad. Sci., 113, 11770–11775, https://doi.org/10.1073/pnas.1607171113, 2016.

Akagi, S. K., Yokelson, R. J., Wiedinmyer, C., Alvarado, M. J., Reid, J. S., Karl, T., Crounse, J. D., and Wennberg, P. O.: Emission factors for open and domestic biomass burning for use in atmospheric models, Atmos. Chem. Phys., 11, 4039–4072, https://doi.org/10.5194/acp-11-4039-2011, 2011.

Anderson, L., Dix, B., Schnell, J., Yokelson, R., Veefkind, J., Ahmadov, R., and de Gouw, J.: Analyzing the Impact of Evolving Combustion Conditions on the Composition of Wildfire Emissions Using Satellite Data, Geophys. Res. Lett., 50, https://doi.org/10.1029/2023GL105811, 2023.

Andreae, M. O.: Emission of trace gases and aerosols from biomass burning – an updated assessment, Atmos. Chem. Phys., 19, 8523–8546, https://doi.org/10.5194/acp-19-8523-2019, 2019.

Boer, M. M., Resco de Dios, V., and Bradstock, R. A.: Unprecedented burn area of Australian mega forest fires, Nat. Clim. Change, 10, 171–172, https://doi.org/10.1038/s41558-020-0716-1, 2020.

Bond, T. C., Doherty, S. J., Fahey, D. W., Forster, P. M., Berntsen, T., DeAngelo, B. J., Flanner, M. G., Ghan, S., Kärcher, B., Koch, D., Kinne, S., Kondo, Y., Quinn, P. K., Sarofim, M. C., Schultz, M. G., Schulz, M., Venkataraman, C., Zhang, H., Zhang, S., Bellouin, N., Guttikunda, S. K., Hopke, P. K., Jacobson, M. Z., Kaiser, J. W., Klimont, Z., Lohmann, U., Schwarz, J. P., Shindell, D., Storelvmo, T., Warren, S. G., and Zender, C. S.: Bounding the role of black carbon in the climate system: A scientific assessment, J. Geophys. Res. Atmos., 118, 5380–5552, https://doi.org/10.1002/jgrd.50171, 2013.

Borsdorff, T., aan de Brugh, J., Schneider, A., Lorente, A., Birk, M., Wagner, G., Kivi, R., Hase, F., Feist, D. G., Sussmann, R., Rettinger, M., Wunch, D., Warneke, T., and Landgraf, J.: Improving the TROPOMI CO data product: update of the spectroscopic database and destriping of single orbits, Atmos. Meas. Tech., 12, 5443–5455, https://doi.org/10.5194/amt-12-5443-2019, 2019.

Dix, B.: barbarakdix1200/Smoke-Plume-Processing: v1.0.0 - Version accompanying manuscript submission (Version v1.0) [Computer software]. Zenodo. https://doi.org/10.5281/zenodo.22036261, 2026

Fredrickson, C. D., Theys, N., and Thornton, J. A.: Satellite Evidence of HONO/NO2 Increase with Fire Radiative Power, Geophys. Res. Lett., 50, e2023GL103836, https://doi.org/10.1029/2023GL103836, 2023.

Friedl, M., D. Sulla-Menashe. MODIS/Terra+Aqua Land Cover Type Yearly L3 Global 0.05Deg CMG V061. 2022, distributed by NASA EOSDIS Land Processes DAAC, https://doi.org/10.5067/MODIS/MCD12C1.061. Accessed 2021-07-21.

van Geffen, J., Eskes, H., Compernolle, S., Pinardi, G., Verhoelst, T., Lambert, J.-C., Sneep, M., ter Linden, M., Ludewig, A., Boersma, K. F., and Veefkind, J. P.: Sentinel-5P TROPOMI NO2 retrieval: impact of version v2.2 improvements and comparisons with OMI and ground-based data, Atmos. Meas. Tech., 15, 2037–2060, https://doi.org/10.5194/amt-15-2037-2022, 2022.

https://doi.org/10.5194/egusphere-2026-5052
Preprint. Discussion started: 8 September 2026


Griffin, D., McLinden, C. A., Dammers, E., Adams, C., Stockwell, C. E., Warneke, C., Bourgeois, I., Peischl, J., Ryerson, T. B., Zarzana, K. J., Rowe, J. P., Volkamer, R., Knote, C., Kille, N., Koenig, T. K., Lee, C. F., Rollins, D., Rickly, P. S., Chen, J., Fehr, L., Bourassa, A., Degenstein, D., Hayden, K., Mihele, C., Wren, S. N., Liggio, J., Akingunola, A., and Makar, P.: Biomass burning nitrogen dioxide emissions derived from space with TROPOMI: methodology and validation, Atmos. Meas. Tech., 14, 7929–7957, https://doi.org/10.5194/amt-14-7929-2021, 2021.

Griffin, D., Chen, J., Anderson, K., Makar, P., McLinden, C. A., Dammers, E., and Fogal, A.: Biomass burning CO emissions: exploring insights through TROPOMI-derived emissions and emission coefficients, Atmos. Chem. Phys., 24, 10159–10186, https://doi.org/10.5194/acp-24-10159-2024, 2024.

Hersbach, H., Bell, B., Berrisford, P., Hirahara, S., Horányi, A., Muñoz-Sabater, J., Nicolas, J., Peubey, C., Radu, R., Schepers, D., Simmons, A., Soci, C., Abdalla, S., Abellan, X., Balsamo, G., Bechtold, P., Biavati, G., Bidlot, J., Bonavita, M., De Chiara, G., Dahlgren, P., Dee, D., Diamantakis, M., Dragani, R., Flemming, J., Forbes, R., Fuentes, M., Geer, A., Haimberger, L., Healy, S., Hogan, R. J., Hólm, E., Janisková, M., Keeley, S., Laloyaux, P., Lopez, P., Lupu, C., Radnoti, G., de Rosnay, P., Rozum, I., Vamborg, F., Villaume, S., and Thépaut, J.-N.: The ERA5 global reanalysis, Q. J. R. Meteorol. Soc., 146, 1999–2049, https://doi.org/10.1002/qj.3803, 2020.

IPCC: Climate Change 2021: The Physical Science Basis. Contribution of Working Group I to the Sixth Assessment Report of the Intergovernmental Panel on Climate Change, edited by: Masson-Delmotte, V., Zhai, P., Pirani, A., Connors, S. L., Péan, C., Berger, S., Caud, N., Chen, Y., Goldfarb, L., Gomis, M. I., Huang, M., Leitzell, K., Lonnoy, E., Matthews, J. B. R., Maycock, T. K., Waterfield, T., Yelekçi, O., Yu, R., and Zhou, B., Cambridge University Press, Cambridge, United Kingdom and New York, NY, USA, 2391 pp., https://doi.org/10.1017/9781009157896, 2021

Jolly, W. M., Cochrane, M. A., Freeborn, P. H., Holden, Z. A., Brown, T. J., Williamson, G. J., and Bowman, D. M. J. S.: Climate-induced variations in global wildfire danger from 1979 to 2013, Nat. Commun., 6, 7537, https://doi.org/10.1038/ncomms8537, 2015.

Jones, M. W., Abatzoglou, J. T., Veraverbeke, S., Andela, N., Lasslop, G., Forkel, M., Smith, A. J. P., Burton, C., Betts, R. A., van der Werf, G. R., Sitch, S., Canadell, J. G., Santín, C., Kolden, C., Doerr, S. H., and Le Quéré, C.: Global and Regional Trends and Drivers of Fire Under Climate Change, Rev. Geophys., 60, e2020RG000726, https://doi.org/10.1029/2020RG000726, 2022.

Khaykin, S., Legras, B., Bucci, S., Sellitto, P., Isaksen, L., Tencé, F., Bekki, S., Bourassa, A., Rieger, L., Zawada, D., Jumelet, J., and Godin-Beekmann, S.: The 2019/20 Australian wildfires generated a persistent smoke-charged vortex rising up to 35 km altitude, Commun. Earth Environ., 1, 22, https://doi.org/10.1038/s43247-020-00022-5, 2020.

Kleinman, L. I., Sedlacek III, A. J., Adachi, K., Buseck, P. R., Collier, S., Dubey, M. K., Hodshire, A. L., Lewis, E., Onasch, T. B., Pierce, J. R., Shilling, J., Springston, S. R., Wang, J., Zhang, Q., Zhou, S., and Yokelson, R. J.: Rapid evolution of aerosol particles and their optical properties downwind of wildfires in the western US, Atmos. Chem. Phys., 20, 13319–13341, https://doi.org/10.5194/acp-20-13319-2020, 2020.

https://doi.org/10.5194/egusphere-2026-5052
Preprint. Discussion started: 8 September 2026


Landgraf, J., aan de Brugh, J., Scheepmaker, R., Borsdorff, T., Hu, H., Houweling, S., Butz, A., Aben, I., and Hasekamp, O.: Carbon monoxide total column retrievals from TROPOMI shortwave infrared measurements, Atmos. Meas. Tech., 9, 4955–4975, https://doi.org/10.5194/amt-9-4955-2016, 2016.

Laurent, P., Mouillot, F., Moreno, M. V., Yue, C., and Ciais, P.: Varying relationships between fire radiative power and fire size at a global scale, Biogeosciences, 16, 275–288, https://doi.org/10.5194/bg-16-275-2019, 2019.

Palm, B. B., Peng, Q., Fredrickson, C. D., Lee, B. H., Garofalo, L. A., Pothier, M. A., Kreidenweis, S. M., Farmer, D. K., Pokhrel, R. P., Shen, Y., Murphy, S. M., Permar, W., Hu, L., Campos, T. L., Hall, S. R., Ullmann, K., Zhang, X., Flocke, F., Fischer, E. V., and Thornton, J. A.: Quantification of organic aerosol and brown carbon evolution in fresh wildfire plumes, Proc. Natl. Acad. Sci., 117, 29469–29477, https://doi.org/10.1073/pnas.2012218117, 2020.

Reid, C. E., Brauer, M., Johnston, F. H., Jerrett, M., Balmes, J. R., and Elliott, C. T.: Critical Review of Health Impacts of Wildfire Smoke Exposure, Environ. Health Perspect., 124, 1334–1343, https://doi.org/10.1289/ehp.1409277, 2016.

Reid, J. S., Koppmann, R., Eck, T. F., and Eleuterio, D. P.: A review of biomass burning emissions part II: intensive physical properties of biomass burning particles, Atmos. Chem. Phys., 5, 799–825, https://doi.org/10.5194/acp-5-799-2005, 2005a.

Reid, J. S., Eck, T. F., Christopher, S. A., Koppmann, R., Dubovik, O., Eleuterio, D. P., Holben, B. N., Reid, E. A., and Zhang, J.: A review of biomass burning emissions part III: intensive optical properties of biomass burning particles, Atmos. Chem. Phys., 5, 827–849, https://doi.org/10.5194/acp-5-827-2005, 2005b.

Rowe, J. P., Zarzana, K. J., Kille, N., Borsdorff, T., Goudar, M., Lee, C. F., Koenig, T. K., Romero-Alvarez, J., Campos, T., Knote, C., Theys, N., Landgraf, J., and Volkamer, R.: Carbon Monoxide in Optically Thick Wildfire Smoke: Evaluating TROPOMI Using CU Airborne SOF Column Observations, ACS Earth Space Chem., 6, 1799–1812, https://doi.org/10.1021/acsearthspacechem.2c00048, 2022.

Schroeder, W., Oliva, P., Giglio, L., and Csiszar, I. A.: The New VIIRS 375 m active fire detection data product: Algorithm description and initial assessment, Remote Sens. Environ., 143, 85–96, https://doi.org/10.1016/j.rse.2013.12.008, 2014.

Seager, R., Hooks, A., Williams, A. P., Cook, B., Nakamura, J., and Henderson, N.: Climatology, Variability, and Trends in the U.S. Vapor Pressure Deficit, an Important Fire-Related Meteorological Quantity, J. Appl. Meteorol. Climatol., 54, 1121–1141, https://doi.org/10.1175/JAMC-D-14-0321.1, 2015.

Torres, O., Ahn, C., and Chen, Z.: Improvements to the OMI near-UV aerosol algorithm using A-train CALIOP and AIRS observations, Atmos. Meas. Tech., 6, 3257–3270, https://doi.org/10.5194/amt-6-3257-2013, 2013.

Torres, O., Jethva, H., Ahn, C., Jaross, G., and Loyola, D. G.: TROPOMI aerosol products: evaluation and observations of synoptic-scale carbonaceous aerosol plumes during 2018–2020, Atmos. Meas. Tech., 13, 6789–6806, https://doi.org/10.5194/amt-13-6789-2020, 2020.

Veefkind, J. P., Aben, I., McMullan, K., Förster, H., de Vries, J., Otter, G., Claas, J., Eskes, H. J., de Haan, J. F., Kleipool, Q., van Weele, M., Hasekamp, O., Hoogeveen, R., Landgraf, J., Snel, R., Tol, P., Ingmann, P., Voors, R., Kruizinga, B., Vink, R., Visser, H., and Levelt, P. F.: TROPOMI on the ESA Sentinel-5 Precursor: A GMES mission for global observations of the

https://doi.org/10.5194/egusphere-2026-5052
Preprint. Discussion started: 8 September 2026


atmospheric composition for climate, air quality and ozone layer applications, Remote Sens. Environ., 120, 70–83, https://doi.org/10.1016/j.rse.2011.09.027, 2012.

van der Velde, I. R., van der Werf, G. R., Houweling, S., Eskes, H. J., Veefkind, J. P., Borsdorff, T., and Aben, I.: Biomass burning combustion efficiency observed from space using measurements of CO and NO2 by the TROPOspheric Monitoring Instrument (TROPOMI), Atmos. Chem. Phys., 21, 597–616, https://doi.org/10.5194/acp-21-597-2021, 2021.

Warneke, C., Schwarz, J. P., Dibb, J., Kalashnikova, O., Frost, G., Al-Saad, J., Brown, S. S., Brewer, Wm. A., Soja, A., Seidel, F. C., Washenfelder, R. A., Wiggins, E. B., Moore, R. H., Anderson, B. E., Jordan, C., Yacovitch, T. I., Herndon, S. C., Liu, S., Kuwayama, T., Jaffe, D., Johnston, N., Selimovic, V., Yokelson, R., Giles, D. M., Holben, B. N., Goloub, P., Popovici, I., Trainer, M., Kumar, A., Pierce, R. B., Fahey, D., Roberts, J., Gargulinski, E. M., Peterson, D. A., Ye, X., Thapa, L. H., Saide, P. E., Fite, C. H., Holmes, C. D., Wang, S., Coggon, M. M., Decker, Z. C. J., Stockwell, C. E., Xu, L., Gkatzelis, G., Aikin, K., Lefer, B., Kaspari, J., Griffin, D., Zeng, L., Weber, R., Hastings, M., Chai, J., Wolfe, G. M., Hanisco, T. F., Liao, J., Campuzano Jost, P., Guo, H., Jimenez, J. L., Crawford, J., and Team, T. F.-A. S.: Fire Influence on Regional to Global Environments and Air Quality (FIREX-AQ), J. Geophys. Res. Atmos., 128, e2022JD037758, https://doi.org/10.1029/2022JD037758, 2023.